

Linear gyrokinetic simulations of reversed shear Alfvén eigenmodes and ion temperature gradient modes in DIII-D tokamak

Hongyu WANG (王虹宇)^{1,2}, Pengfei LIU (刘鹏飞)², Zhihong LIN (林志宏)² and Wenlu ZHANG (张文禄)³

¹Fusion Simulation Center, Peking University, Beijing 100871, People's Republic of China

²Department of Physics and Astronomy, University of California, Irvine, CA 92697, United States of America

³Institute of Physics, Chinese Academy of Sciences, Beijing 100190, People's Republic of China

E-mail: zhihongl@uci.edu

Received 28 July 2020, revised 5 November 2020

Accepted for publication 6 November 2020

Published 3 December 2020



CrossMark

Abstract

Global linear gyrokinetic simulations using realistic DIII-D tokamak geometry and plasma profiles find co-existence of unstable reversed shear Alfvén eigenmodes (RSAE) with low toroidal mode number n and electromagnetic ion temperature gradient (ITG) instabilities with higher toroidal mode number n . For intermediate $n = [10, 12]$, RSAE and ITG co-exist and overlap weakly in the radial domain with similar growth rates but different real frequencies. Both RSAE and ITG growth rates decrease less than 5% when compressible magnetic perturbations are neglected in the simulations. The ITG growth rates increase less than 7% when fast ions are not included in the simulations. Finally, the effects of trapped electrons on the RSAE are negligible.

Keywords: fast ions, gyrokinetic simulation, reversed shear Alfvén eigenmodes, microturbulence

(Some figures may appear in colour only in the online journal)

1. Introduction

Energetic particle (EP) confinement is a key physical issue for burning plasma experiment in ITER [1, 2] since ignition relies on self-heating by energetic fusion products [3], i.e. α -particles. The EP population in current tokamaks can be produced by auxiliary heating such as neutral beam injection [4] and radio frequency heating [5]. EP pressure gradients can readily excite mesoscale EP instabilities such as the Alfvén eigenmodes (AE) [6], which can drive large EP transport, degrade overall plasmas confinement, and threaten the machines' integrity [7]. Because EP constitutes a significant fraction of the plasma energy density, EP could influence thermal particle dynamics including the microturbulence [8, 9] responsible for turbulent transport of thermal particles and the macroscopic

magnetohydrodynamic (MHD) modes potentially leading to disastrous disruptions [10]. In return, microturbulence and MHD modes can affect EP confinement [11, 12].

Thanks to recent progress in developing comprehensive EP simulation codes and understanding basic EP physics, gyrokinetic turbulence simulation has been successfully established as a necessary paradigm shift for studying EP confinement [13–16]. Integrated simulation incorporating multiple physical processes and disparate temporal-spatial scales becomes available now to address new challenges in the EP physics such as the coupling of EP-driven AE turbulence with thermal particles-driven microturbulence and macroscopic MHD modes. The fully self-consistent gyrokinetic turbulence simulation needs to treat both EP and thermal particles on the same footing to address the kinetic effects of

thermal particles and the cross-scale couplings between microturbulence, EP turbulence, and MHD modes.

Toward such an integrated simulation of EP coupling with thermal particles, we have initiated comprehensive simulations of turbulent transport by low frequency electromagnetic instabilities (including AE and microturbulence) in a reversed shear geometry of DIII-D tokamak with fast ions [17] by using the gyrokinetic toroidal code (GTC) [18]. GTC has been extensively verified and validated for global simulations of AE [13–16, 19] and microturbulence [11, 18, 20–22]. As the first step in the integrated simulations of EP, we study the linear properties of these electromagnetic instabilities, which could provide a foundation for the next step of nonlinear simulations of multiple physical processes.

In this paper, linear global GTC simulations using realistic DIII-D magnetic geometry and plasma profiles with kinetic electrons, thermal ions and fast ions find co-existence of unstable reversed shear Alfvén eigenmodes (RSAE) with low toroidal mode number $n < 10$ and ion temperature gradient (ITG) instabilities with higher toroidal mode number $n > 12$. For intermediate toroidal modes $n = [10, 12]$, RSAE and ITG eigenmodes overlap weakly in the radial domain with similar growth rates but different real frequencies. The RSAE polarization is very close to ideal Alfvénic state, while the ITG polarization is closer to electrostatic but with significant magnetic perturbations.

Our simulations represent the first gyrokinetic study for the effects of compressible magnetic perturbations δB_{\parallel} on the RSAE in this DIII-D experiment. GTC simulations with δB_{\parallel} have been verified for ITG, collisionless trapped electron mode, and kinetic ballooning mode [23, 24]. Although many gyrokinetic codes have the capability for including δB_{\parallel} in the simulations of microturbulence, most of gyrokinetic simulations of RSAE neglect δB_{\parallel} [9, 13, 16, 25–27]. On the other hand, most of hybrid MHD-gyrokinetic codes do not separate parallel and perpendicular magnetic perturbations [13, 16, 28–30]. Therefore, the effects of δB_{\parallel} on RSAE are not well understood. The δB_{\parallel} can be important for low frequency instabilities since it cancels out the stabilizing ‘drift-reversal’ effects of the guiding center ∇B drifts associated with the perpendicular diamagnetic current in finite- β plasmas [31]. Gyrokinetic flux-tube simulations using GS2 code [32] for ITG in a simple s - α geometry find that the ITG growth rate decreases by a factor of 3 when δB_{\parallel} is neglected in the simulations. However, global GTC simulations using similar geometry and plasma β find that the ITG growth rate decreases less than 5% when δB_{\parallel} is neglected in the simulations [24]. In the current GTC simulations using realistic DIII-D magnetic geometry and plasma profiles, both RSAE and ITG growth rates decrease less than 5% when δB_{\parallel} is neglected in the simulations. Furthermore, GTC simulations find that the effects of trapped electrons on the RSAE are negligible.

Our simulations also clarify the effects of fast ions on the ITG in this DIII-D experiment. It is well-known that the adiabatic responses of electrons and fast ions can have stabilizing effects

on the ITG due to the finite- β stabilization [33] and that fast ion drift-bounce and precessional resonances [6, 34, 35] can stabilize or destabilize low frequency drift-Alfvén instabilities, depending on specific plasma parameters. In the current GTC simulations using realistic DIII-D magnetic geometry and plasma profiles, the ITG growth rate increases less than 7% when fast ions are not included in the simulations. Finally, GTC simulations find that the ITG eigenmodes become stable if electrons are assumed to be adiabatic, i.e. by neglecting kinetic effects of trapped electrons.

The rest of the paper is organized as follows. In section 2, GTC electromagnetic simulation model with compressible magnetic perturbations δB_{\parallel} is described. The simulation results are discussed in section 3. The conclusions are provided in section 4.

2. Gyrokinetic electromagnetic simulation model

By means of parallel symplectic gyrocenter model [36], the nonlinear gyrokinetic equation used in GTC to study low frequency mode could be written as [24, 37],

$$\frac{d}{dt} f_{\alpha}(\mathbf{X}, \mu, v_{\parallel}, t) = \left[\frac{\partial}{\partial t} + \dot{\mathbf{X}} \cdot \nabla + \dot{v}_{\parallel} \frac{\partial}{\partial v_{\parallel}} - C_{\alpha} \right] f_{\alpha} = 0$$

in which

$$\dot{\mathbf{X}} = v_{\parallel} \frac{\mathbf{B}_0 + \nabla \times (\lambda \mathbf{B}_0)}{B_0} + \mathbf{v}_E + \mathbf{v}_d + \mathbf{v}_{b\parallel}$$

$$\dot{v}_{\parallel} = -\frac{1}{m_{\alpha}} \frac{\mathbf{B}^*}{B_0} \cdot (\mu \nabla B_0 + Z_{\alpha} \nabla \delta \phi) - \frac{Z_{\alpha}}{m_{\alpha} c} \frac{\partial \delta A_{\parallel}}{\partial t}$$

$f_{\alpha}(\mathbf{X}, \mu, v_{\parallel}, t)$ is distribution function, with \mathbf{X} the gyrocenter position, μ the magnetic momentum, v_{\parallel} the parallel velocity, α the particle species (thermal ion, fast ion, or electron), Z_{α} the particle charge, and m_{α} the particle mass. Collision operator C_{α} is set to be 0 in this work. \mathbf{B}_0 is the equilibrium magnetic field, $\mathbf{B}^* = \mathbf{B}_0 + (B_0 v_{\parallel} / \Omega_{\alpha}) \nabla \times \mathbf{b}_0 + \nabla \times (\lambda \mathbf{B}_0)$, $\mathbf{b}_0 = \frac{\mathbf{B}_0}{B_0}$, $\lambda = \delta A_{\parallel} / B_0$, and $\Omega_{\alpha} = \frac{Z_{\alpha} B_0}{m_{\alpha} c}$ cyclone frequency with c the light speed. $\delta \phi$, δA_{\parallel} , and δB_{\parallel} are, respectively, perturbed electrostatic potential, perturbed vector potential, and perturbed parallel magnetic field. \mathbf{v}_E , \mathbf{v}_d and $\mathbf{v}_{b\parallel}$ are, respectively, $\mathbf{E} \times \mathbf{B}$ drift velocity, magnetic drift velocity of equilibrium magnetic fields, and magnetic drift velocity of perturbed parallel magnetic field δB_{\parallel} .

In order to reduce the particle noise in simulations, δf -method [38] is used for thermal ions and fast ions, by decomposing the distribution function f_{α} of species α into an equilibrium part $f_{0\alpha}$ and a perturbed part δf_{α} , i.e. $f_{\alpha} = f_{0\alpha} + \delta f_{\alpha}$. The equilibrium part is defined by:

$$\left[\frac{\partial}{\partial t} + (v_{\parallel} \mathbf{b}_0 + \mathbf{v}_d) \cdot \nabla - \frac{1}{m_{\alpha}} \frac{\mathbf{B}_0 + B_0 v_{\parallel} \nabla \times \mathbf{b}_0 / \Omega_{\alpha}}{B_0} \cdot \mu \nabla B_0 \frac{\partial}{\partial v_{\parallel}} \right] f_{0\alpha} = 0.$$

The perturbed part is solved by using a particle weight variable $w_\alpha = \delta f_\alpha / f_\alpha$, which satisfies:

$$\begin{aligned} \frac{d}{dt} w_\alpha = (1 - w_\alpha) & \left[-\frac{c\mathbf{b}_0}{B_0} \times \nabla \left(\delta\phi - v_{\parallel} \delta A_{\parallel} + \frac{\mu}{Z_\alpha} \langle \delta B_{\parallel} \rangle \right) \right. \\ & \cdot \nabla \ln f_{\alpha 0}|_{v_{\perp}} - \frac{Z_\alpha v_{\parallel} \mathbf{b}_0}{T_\alpha} \cdot \nabla \phi_{\text{eff}} - \frac{\mu v_{\parallel} \mathbf{b}_0 \cdot \nabla \langle \delta B_{\parallel} \rangle}{T_\alpha} \\ & \left. + \frac{Z_\alpha \mathbf{v}_d}{T_\alpha} \cdot \nabla \left(\delta\phi + \frac{\mu}{Z_\alpha} \langle \delta B_{\parallel} \rangle \right) \right], \end{aligned} \quad (1)$$

where $\langle \delta B_{\parallel} \rangle = \frac{1}{\pi \rho^2} \int_0^\rho r dr \int_0^{2\pi} \delta B_{\parallel} d\zeta$ is the gyro-surface averaging of the perturbed parallel magnetic field [39] with ρ the gyroradius and r the radial direction in local cylindrical coordinate.

Particle density n_α and parallel velocity $u_{\parallel\alpha}$ are moments of distribution functions in velocity space:

$$n_\alpha = \int d\mathbf{v} f_\alpha$$

$$n_\alpha u_{\parallel\alpha} = \int d\mathbf{v} f_\alpha v_{\parallel\alpha}$$

where

$$\int d\mathbf{v} = \frac{2\pi B_0}{m} \int dv_{\parallel} d\mu.$$

The electron dynamics is described by the fluid-kinetic hybrid model [37], which separates the electron response into a dominant adiabatic part and a higher order nonadiabatic part due to the small electron ion mass ratio, i.e. $f_e = f_{e0} + \delta f_e^0 + \delta h_e$. The equilibrium distribution f_{e0} is defined by equation (4). The adiabatic part δf_e^0 is defined as:

$$\delta f_e^0 = \frac{e\phi_{\text{eff}}}{T_e} f_{e0} - \frac{\mu}{T_e} \delta B_{\parallel} f_{e0} + \frac{\partial f_{e0}}{\partial \psi_0}|_{v_{\perp}} \delta \psi,$$

where,

$$\frac{e\phi_{\text{eff}}}{T_e} = \frac{\delta n_e}{n_0} + \frac{\delta B_{\parallel}}{B_0} + \frac{1}{n_0} \frac{\partial n_0}{\partial \psi_0} \delta \psi \quad (2)$$

$$\frac{\partial \delta \psi}{\partial t} = -c \frac{\partial}{\partial \alpha_0} (\phi_{\text{eff}} - \delta \phi) \quad (3)$$

ψ , θ , ζ are, respectively, poloidal flux, poloidal angle, and toroidal angle in magnetic coordinates, and $\alpha = q(\psi)\theta - \zeta$ is the magnetic field line label. The Clebsch representation for the toroidal magnetic field is $\mathbf{B} = \mathbf{B}_0 + \delta \mathbf{B} = \nabla(\psi_0 + \delta \psi) \times \nabla(\alpha_0 + \delta \alpha)$, in which the magnetic flux perturbation $\delta \psi$ is calculated by assuming $\nabla \times \mathbf{B}_0 = 0$. Effective scalar potential is $\phi_{\text{eff}} = \phi_{\text{ind}} + \delta \phi$, and $\frac{\partial}{\partial t} \delta A_{\parallel} = c\mathbf{b}_0 \cdot \nabla \phi_{\text{ind}}$.

The nonadiabatic part δh_e is solved by using an electron weight $w_e = \delta h_e / f_e$, which satisfies:

$$\begin{aligned} Lw_e = & \left(1 - \frac{\delta f_e^0}{f_{e0}} - w_e \right) \left[-\frac{\partial}{\partial t} \frac{\delta f_e^0}{f_{e0}} - \mathbf{v}_E \cdot \nabla \ln f_{e0}|_{v_{\perp}} \right. \\ & \left. + \frac{c\mu}{eB_0} \mathbf{b}_0 \times \nabla \delta B_{\parallel} \cdot \nabla \ln f_{e0}|_{v_{\perp}} \right. \\ & \left. - \mathbf{v}_d \cdot \nabla \left(\frac{e(\phi_{\text{eff}} - \delta \phi)}{T_e} + \frac{\delta \psi}{f_{e0}} \frac{\partial f_{e0}}{\partial \psi_0}|_{v_{\perp}} \right) \right]. \end{aligned} \quad (4)$$

The perturbed electron density is calculated by the continuity equation:

$$\begin{aligned} \frac{\partial \delta n_e}{\partial t} + B_0 \mathbf{b}_0 \cdot \nabla \left(\frac{n_0 \delta u_{\parallel e}}{B_0} \right) + B_0 \mathbf{v}_E \cdot \nabla \left(\frac{n_0}{B_0} \right) \\ - n_0 (\mathbf{v}_* + \mathbf{v}_E) \cdot \frac{\nabla B_0}{B_0} + \delta \mathbf{B}_{\perp} \cdot \nabla \left(\frac{n_0 u_{\parallel e 0}}{B_0} \right) - \frac{c \nabla \times \mathbf{B}_0}{eB_0^2} \\ \cdot \left[\nabla \delta P_{e\parallel} + \frac{(\delta P_{e\perp} - \delta P_{e\parallel}) \nabla B_0}{B_0} - en_0 \nabla \delta \phi \right] \\ + \nabla \cdot \left(\frac{c \delta P_{e\parallel} \mathbf{b}_0 \nabla \times \mathbf{b}_0 \cdot \mathbf{b}_0}{eB_0} \right) + \delta \mathbf{B}_{\perp} \cdot \nabla \left(\frac{n_0 \delta u_{\parallel e}}{B_0} \right) \\ + B_0 \mathbf{v}_E \cdot \nabla \left(\frac{\delta n_e}{B_0} \right) + \frac{c \delta n_e}{B_0^2} (\nabla \times \mathbf{B}_0 + \mathbf{b}_0 \times \nabla B_0) \\ \cdot \nabla \delta \phi - \frac{c \mathbf{b}_0 \times \nabla \delta B_{\parallel}}{e} \cdot \nabla \frac{\delta P_{e\perp} + P_{e0}}{B_0^2} \\ - \frac{c \nabla \times \mathbf{b}_0 \cdot \nabla \delta B_{\parallel}}{eB_0^2} (\delta P_{e\perp} + P_{e0}) = 0, \end{aligned} \quad (5)$$

where

$$\mathbf{v}_* = \frac{1}{n_0 m_e \Omega_e} \mathbf{b}_0 \times \nabla (\delta P_{e\perp} + \delta P_{e\parallel}).$$

The electron pressure is defined as:

$$\delta P_{e\parallel} = en_0 \phi_{\text{eff}} - P_{e0} \frac{\delta B_{\parallel}}{B_0} + \frac{\partial P_{e0}}{\partial \psi_0} \delta \psi + \int m_e v_{e\parallel}^2 \delta h_e d\mathbf{v},$$

$$\delta P_{e\perp} = en_0 \phi_{\text{eff}} - 2P_{e0} \frac{\delta B_{\parallel}}{B_0} + \frac{\partial P_{e0}}{\partial \psi_0} \delta \psi + \int \mu B_{\parallel}^* \delta h_e d\mathbf{v},$$

and the electron parallel flow is calculated from the Ampere's law:

$$en_e \delta u_{e\parallel} = \frac{c}{4\pi} \nabla_{\perp}^2 \delta A_{\parallel} + Z_i n_i \delta u_{\parallel i}. \quad (6)$$

These electron equations are closed by the gyrokinetic Poisson's equation, perpendicular Ampere's law, and Ohm's law for $\delta \phi$, δB_{\parallel} and δA_{\parallel} , respectively,

$$\sum_{\alpha} \frac{Z_{\alpha} n_{\alpha 0}}{T_{\alpha}} (\delta \phi - \tilde{\delta \phi}) = \sum_{\alpha} Z_i \delta n_{\alpha} - e \delta n_e, \quad (7)$$

$$\begin{aligned} \frac{\delta B_{\parallel}}{B_0} + \frac{\beta_e q_e \delta \phi}{2 T_e} + \sum_{\alpha} \frac{\beta_{\alpha}}{2} e^{-k_{\perp}^2 \rho_{\alpha}^2} (I_0 - I_1) \frac{Z_{\alpha} \delta \phi}{T_{\alpha}} \\ = -\frac{4\pi}{B_0} \left(\delta P_{e\perp} + \sum_{\alpha} \delta P_{\alpha\perp} \right) \end{aligned} \quad (8)$$

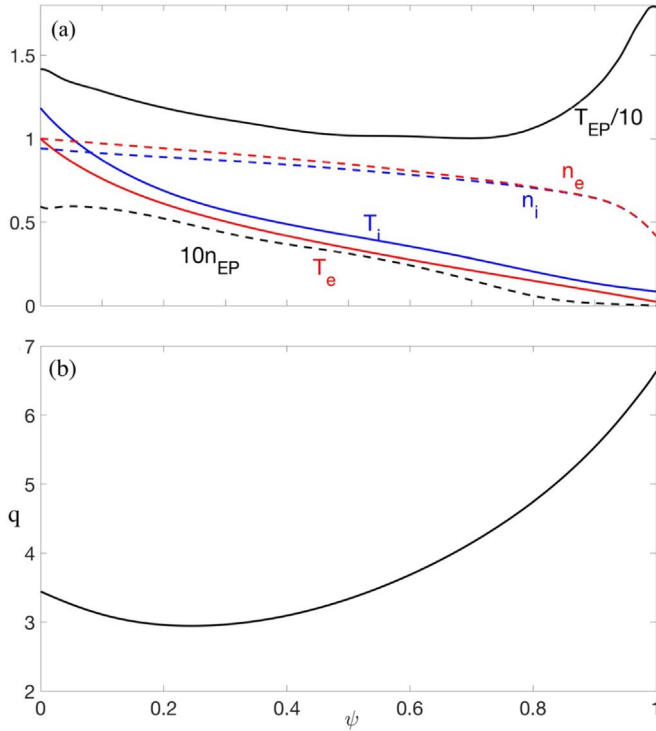


Figure 1. Equilibrium plasma profiles of DIII-D shot #159243 at 805 ms. (a) Radial profiles of densities (dashed lines, normalized to the electron on axis value $n_0 = 3.29 \times 10^{19} \text{ m}^{-3}$) and temperatures (solid lines, normalized to the electron on-axis value $T_{e0} = 1.69 \text{ keV}$) for the electron (red), thermal ion (blue), and fast ion (black). Fast ion density is multiplied by 10 and temperature divided by 10. (b) Radial profile of safety factor q with $q_{\min} = 2.94$ at poloidal flux function $\psi = 0.24 \psi_X$. Data are taken from [16].

$$\frac{\partial \delta A_{\parallel}}{\partial t} = c \mathbf{b}_0 \cdot \nabla (\phi_{\text{eff}} - \delta \phi). \quad (9)$$

In equation (7), $\tilde{\delta \phi}$ represents the double gyroaveraged electrostatic potential [40]. In equation (8), $\beta_{\alpha} = \frac{8\pi n_{\alpha 0} T_{\alpha 0}}{B_0^2}$, I_0 and I_1 represent Bessel functions. Equations (1)–(9) are a set of closed nonlinear system for low frequency modes. This simulation model incorporates physics of drift wave, shear Alfvén wave, and slow magnetoacoustic wave in general toroidal geometry.

3. Simulation results

In this section, we use the GTC model described in section 2 to simulate low frequency electromagnetic instabilities in the DIII-D tokamak shot #159243 at $t = 805 \text{ ms}$ [17]. GTC simulations use the same magnetic geometry and plasma profiles of DIII-D as those in a verification and validation benchmark of RSAE [16]. The density and temperature profiles for the electrons, thermal ions, and fast ions are shown in figure 1(a). For simplicity, Maxwellian distribution function is assumed for both fast ions and thermal particles in this work (effects of slowing-down distribution function will be studied in the future work). This is a reversed shear discharge

with the minimum safety factor of $q_{\min} = 2.94$ at the poloidal flux function $\psi = 0.24 \psi_X$ (ψ_X is the poloidal flux function at the magnetic separatrix) as shown in figure 1(b). Some key plasma parameters are as follows: major radius $R_0 = 1.72 \text{ m}$, on axis electron temperature $T_e = 1.69 \text{ keV}$, density $n_e = 3.29 \times 10^{19} \text{ m}^{-3}$, magnetic field $B_0 = 1.99 \text{ T}$, and total beta 0.9%. At $\psi = 0.68 \psi_X$, the characteristic lengths of density and temperature gradients are $R_0/L_{T_i} = 13.5$, $R_0/L_{n_e} = 2.64$, $R_0/L_{T_e} = 14.1$, $R_0/L_{n_f} = 42.39$, and $R_0/L_{T_f} = 5.25$, with $L_{n\alpha} = \left(\frac{d \ln n_{\alpha}}{dr}\right)^{-1}$ and $L_{T\alpha} = \left(\frac{d \ln T_{\alpha}}{dr}\right)^{-1}$, and the minor radius r is defined as the distance from magnetic axis on the outer mid-plane. The boundaries of the radial simulation domain are $\psi_{\text{inner}} = 0.02 \psi_X$ and $\psi_{\text{outer}} = 0.95 \psi_X$ for the ITG simulations, and $\psi_{\text{outer}} = 0.88 \psi_X$ for the RSAE simulations. The simulation time step size is $\Delta t = 0.0025 R_0 / C_s$, with $C_s = \sqrt{T_e / m_i}$, and $C_s / R_0 = 1.24 \times 10^5 \text{ s}^{-1}$. For linear simulations, we use 250 radial grid points, 1500 poloidal grid points, 32 parallel grid points, and 100 particles per cell each for electrons, thermal ions and fast ions.

The fast ion density and temperature gradients have been shown [16] to drive an unstable RSAE near q_{\min} . The strong temperature gradients of thermal ions and electrons are expected to excite the ITG instabilities. To study these instabilities, we have performed a series of linear simulations, each with a single toroidal mode number n . We have found unstable toroidal modes for $n > 2$. The branches of these modes can be identified by the frequencies and polarizations. The real frequencies and growth rates for these unstable modes are shown in figure 2(a). For $n = [3, 9]$, the instabilities are dominated by the RSAE driven by the fast ions. For $n \geq 10$, the instabilities are dominated by the ITG excited by the thermal ions and electrons. A sub-dominant RSAE can also be identified for $n = [10, 12]$, where the RSAE growth rates are smaller than the ITG growth rates. Both RSAE and ITG propagate in the ion diamagnetic direction (i.e. negative real frequencies). The RSAE real frequency increases with the toroidal mode number n until $n = 8$, where it reaches a plateau. The RSAE real frequencies are much larger than the growth rates, indicating a resonant excitation by the fast ions. The most unstable RSAE with $n = 4$ (which corresponds to $k_{\theta} \rho_f = 0.51$) has a growth rate of $\gamma_4 = 3.24 \times 10^4 \text{ s}^{-1}$ and real frequency $f_4 = \frac{\omega_4}{2\pi} = 6.86 \times 10^4 \text{ s}^{-1}$. The ITG growth rates are comparable to the real frequencies for all the n -modes, indicating mostly non-resonant instabilities due to the strong temperature gradients of the thermal ions and electrons. The most unstable ITG with $n = 20$ (which corresponds to $k_{\theta} \rho_i = 0.33$) has a growth rate of $\gamma_{20} = 5.23 \times 10^4 \text{ s}^{-1}$ and real frequency $f_{20} = \frac{\omega_{20}}{2\pi} = 1.37 \times 10^4 \text{ s}^{-1}$, i.e. $\gamma_{20} \sim \omega_{20}$. The RSAE and ITG growth rates decrease for higher n modes due to the finite Larmor radius effects of the fast ions and thermal ions, respectively.

Besides the fact that the RSAEs have much higher frequencies than the ITGs, they have different polarizations. The RSAE polarization is Alfvénic, where the inductive parallel electric fields are nearly canceled out by the electrostatic parallel electric fields, i.e. $\phi_{\text{eff}} \ll \delta \phi$. On the other hand, the

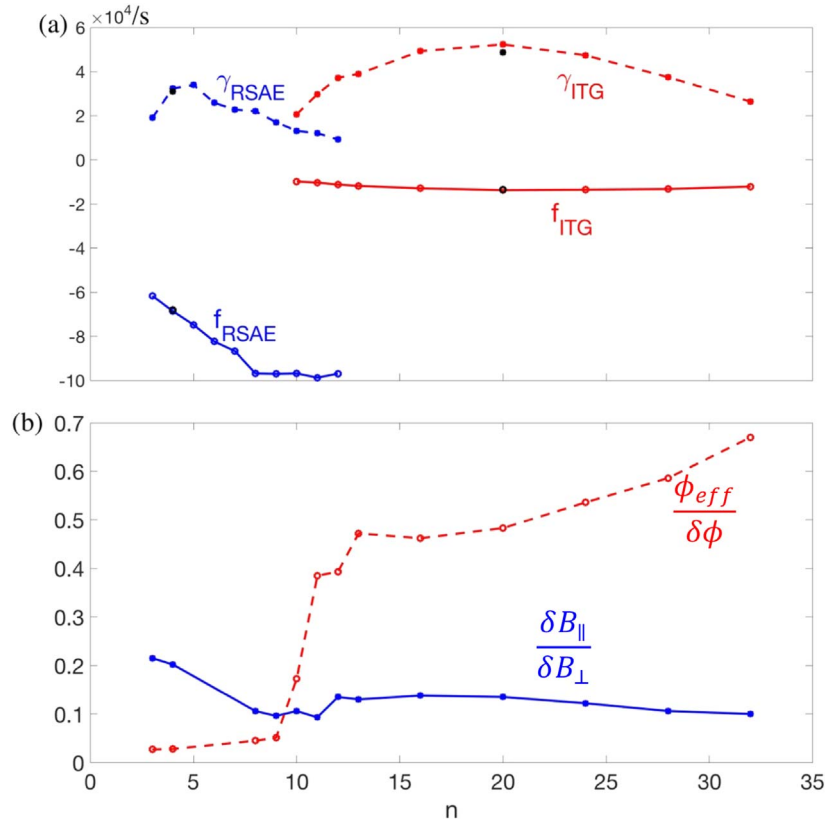


Figure 2. Dispersion relation and polarization: toroidal mode number n dependence of (a) growth rates γ (dashed lines) and frequencies $f = \omega/2\pi$ (solid lines) for RSAE (blue) and ITG (red), and (b) ratio of volume-averaged $\delta B_{\parallel}/\delta B_{\perp}$ (blue solid line) and $\phi_{\text{eff}}/\delta\phi$ (red dashed line). Black cycles and black squares are, respectively, frequencies and growth rates from simulations without δB_{\parallel} .

ITG polarization is electrostatic, where the net parallel electric fields are dominated by the electrostatic components, i.e. $\phi_{\text{eff}} \sim \delta\phi$. The ratio of effective potential over electrostatic potential $\phi_{\text{eff}}/\delta\phi$ is shown in figure 2(b). For toroidal modes $n = [3, 9]$, the ratio $\phi_{\text{eff}}/\delta\phi < 5\%$, which indicates that unstable RSAE is indeed Alfvénic. The ratio $\phi_{\text{eff}}/\delta\phi$ increases for larger toroidal mode number n . For $n > 12$, the ratio $\phi_{\text{eff}}/\delta\phi > 40\%$, which indicates that ITG instability is closer to electrostatic but with significant electromagnetic perturbations.

The generation and effects of compressible magnetic perturbations have been studied. The ratio of perturbed parallel magnetic field over perturbed perpendicular magnetic field $\delta B_{\parallel}/\delta B_{\perp}$ is shown in figure 2(b). For the ITG, $\delta B_{\parallel}/\delta B_{\perp} < 15\%$, indicating that δB_{\parallel} is not significantly generated by the ITG with $\beta = 0.9\%$. The ratio $\delta B_{\parallel}/\delta B_{\perp}$ slightly increases for RSAE with smaller n with $\delta B_{\parallel}/\delta B_{\perp} > 20\%$ for $n = 3$ and 4, indicating that the effects of δB_{\parallel} is more strongly generated by the RSAE. Overall, the effects of δB_{\parallel} are not important for both RSAE and ITG since the growth rates only decrease less than 5% and the frequencies barely change when δB_{\parallel} is removed in the simulation of $n = 4$ and $n = 20$ modes, as shown in figure 2(a). We have also studied the effects of fast ions on the ITG and found that the growth rate and frequency of the $n = 20$ ITG increase by less than 7% when the fast ions are not included in the simulations.

We have also studied the effects of trapped electrons on the RSAE and found that the $n = 4$ RSAE growth rate

decreases by less than 1% when trapped electrons are not included in the simulations. On the other hand, GTC simulations find that the ITG mode in this DIII-D discharge becomes stable if electrons are adiabatic, i.e. when kinetic effects of trapped electrons are neglected.

The eigenmode structures for toroidal mode numbers $n = 4$ and $n = 10$ are compared in figure 3. The perturbed electrostatic potential $\delta\phi$ and parallel vector potential δA_{\parallel} for the $n = 4$ RSAE in figures 3(a) and (b) are localized near the q_{min} flux surface with a narrow radial width. The RSAE structure is weakly ballooning and the radial symmetry is broken, i.e. forming triangular shapes due to the non-perturbative effects of fast ions [13, 15, 16, 41]. The phase shift between $\delta\phi$ and δA_{\parallel} is close to $\pi/2$ as expected for the shear Alfvén wave. The structures of the perturbed electrostatic potential $\delta\phi$ and parallel vector potential δA_{\parallel} for the $n = 10$ mode in figures 3(c) and (d) are much more complicated due to the co-existence of RSAE and ITG with similar growth rates. In addition to the RSAE mode still visible around the flux surface with q_{min} , the ITG modes appear in both positive shear (outer) and negative shear (inner) regions [42]. The growth rates of these three modes are similar, however, the frequencies are quite different: the RSAE frequency is much larger than that of the ITG in the outer region (positive shear), as shown in figure 2(a). The ITG in the inner region (negative shear) has the smallest frequency, which is much smaller than

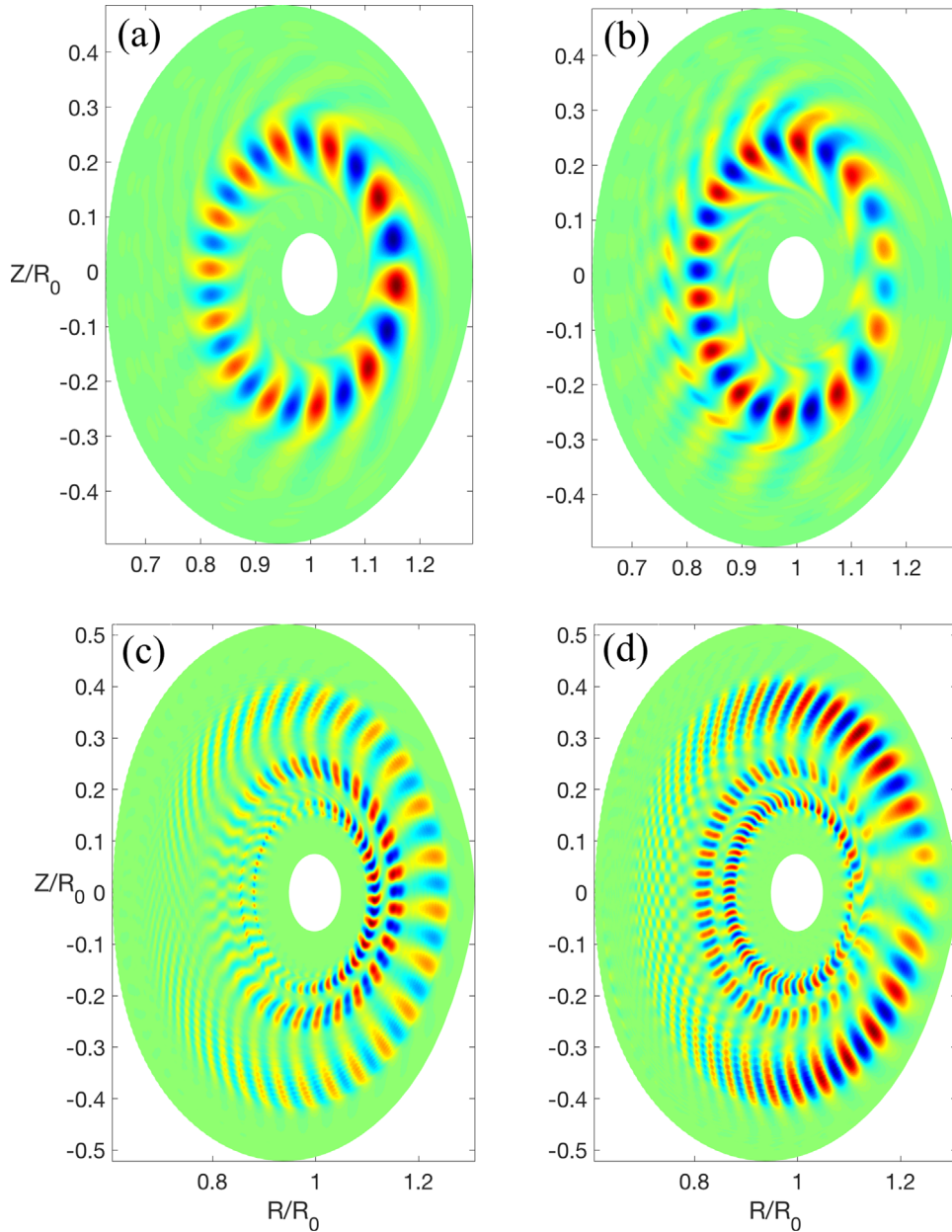


Figure 3. Poloidal mode structures of (a) perturbed electrostatic potential $\delta\phi$ and (b) parallel vector potential $\delta A_{||}$ of RSAE with $n = 4$, and (c) perturbed electrostatic potential and (d) parallel vector potential of ITG with $n = 10$. Red and yellow represent positive values, while blue and cyan represent negative values.

the growth rate. Compared to the $n = 4$ RSAE, the weaker $n = 10$ RSAE has a stronger ballooning structure. The ITG modes are also strong ballooning. The phase shift between $\delta\phi$ and $\delta A_{||}$ is close to $\pi/2$ for both RSAE and ITG eigenmodes. These linear RSAE and ITG eigenmodes overlap weakly in the radial domain. In the future study, we will study the nonlinear interactions of these RSAE and ITG eigenmodes. The spatial overlap of these modes could be even stronger due to turbulence spreading in radial domain [43].

4. Conclusions

In summary, global GTC linear simulations using realistic DIII-D tokamak geometry and plasma profiles with kinetic electrons,

thermal ions, and fast ions find co-existence of unstable RSAE with low toroidal mode number n and ITG instabilities with higher toroidal mode number n . For intermediate toroidal modes $n = [10, 12]$, RSAE and ITG eigenmodes overlap in the radial domain with similar growth rate but different real frequencies. The RSAE polarization is very close to ideal Alfvénic state, while the ITG polarization is closer to electrostatic but with significant magnetic perturbations.

Our simulations represent the first gyrokinetic simulation for the effects of compressible magnetic perturbations $\delta B_{||}$ on the RSAE. In the current GTC simulations using realistic DIII-D magnetic geometry and plasma profiles, both RSAE and ITG growth rates decrease less than 5% when $\delta B_{||}$ is neglected in the simulations. The effects of trapped electrons

on the RSAE are negligible. Furthermore, ITG growth rates increase less than 7% when fast ions are not included in the simulations. Finally, GTC simulations find that the ITG in this DIII-D discharge become stable if electrons are adiabatic, i.e. by neglecting kinetic effects of trapped electrons.

The survey and understanding of the linear properties of these electromagnetic instabilities described in this paper provide a foundation for the next step of fully self-consistent gyrokinetic turbulence simulations treating both fast ions and thermal particles on the same footing to address the kinetic effects of thermal particles and the cross-scale coupling between microturbulence and mesoscale EP turbulence.

Acknowledgments

The authors would like to thank S Taimourzadeh and W W Heidbrink for providing the DIII-D equilibrium data (as published in [16]). We acknowledge technical support by the GTC team. This work was supported by the China National Magnetic Confinement Fusion Science Program (Grant No. 2018YFE0304100), the US Department of Energy, Office of Science, Office of Advanced Scientific Computing Research and Office of Fusion Energy Sciences, and the Scientific Discovery through Advanced Computing (SciDAC) program under Award No. DE-SC0018270 (SciDAC ISEP Center), and the China Scholarship Council (Grant No. 201806010067). This work used resources of the Oak Ridge Leadership Computing Facility at the Oak Ridge National Laboratory (DOE Contract No. DE-AC05-00OR22725) and the National Energy Research Scientific Computing Center (DOE Contract No. DE-AC02-05CH11231).

References

- [1] Chen L and Zonca F 2007 *Nucl. Fusion* **47** S727
- [2] ITER Physics Basis 1999 *Nucl. Fusion* **39** 2137
- [3] Fasoli A et al 2007 *Nucl. Fusion* **47** S264
- [4] Stix T H 1972 *Plasma Phys.* **14** 367
- [5] Fisch N J 1987 *Rev. Mod. Phys.* **59** 175
- [6] Chen L and Zonca F 2016 *Rev. Mod. Phys.* **88** 015008
- [7] Pace D C, Heidbrink W W and Van Zeeland M A 2015 *Phys. Today* **68** 34
- [8] Zonca F et al 2015 *New J. Phys.* **17** 013052
- [9] Bass E M and Waltz R E 2010 *Phys. Plasmas* **17** 112319
- [10] Hender T C et al 2007 *Nucl. Fusion* **47** S128
- [11] Zhang W L, Lin Z H and Chen L 2008 *Phys. Rev. Lett.* **101** 095001
- [12] Tang X et al 2020 *Phys. Plasmas* **27** 032508
- [13] Spong D A et al 2012 *Phys. Plasmas* **19** 082511
- [14] Zhang H S, Lin Z H and Holod I 2012 *Phys. Rev. Lett.* **109** 025001
- [15] Wang Z X et al 2013 *Phys. Rev. Lett.* **111** 145003
- [16] Taimourzadeh S et al 2019 *Nucl. Fusion* **59** 066006
- [17] Collins C S et al 2016 *Phys. Rev. Lett.* **116** 095001
- [18] Lin Z et al 1998 *Science* **281** 1835
- [19] Zhang H S and Lin Z H 2013 *Plasma Sci. Technol.* **15** 969
- [20] Lin Z H et al 2012 *Plasma Sci. Technol.* **14** 1125
- [21] Xiao Y et al 2015 *Phys. Plasmas* **22** 022516
- [22] Fang K S, Bao J and Lin Z H 2019 *Plasma Sci. Technol.* **21** 115102
- [23] Dong G et al 2019 *Phys. Plasmas* **26** 010701
- [24] Dong G et al 2017 *Phys. Plasmas* **24** 081205
- [25] Deng W J et al 2010 *Phys. Plasmas* **17** 112504
- [26] Bass E M and Waltz R E 2013 *Phys. Plasmas* **20** 012508
- [27] Chen Y et al 2018 *Phys. Plasmas* **25** 032304
- [28] Todo Y and Sato T 1998 *Phys. Plasmas* **5** 1321
- [29] Spong D A 2014 *Plasma Fusion Res.* **9** 3403077
- [30] Wang T et al 2020 *Nucl. Fusion* **60** 126032
- [31] Berk H L and Dominguez R R 1977 *J. Plasma Phys.* **18** 31
- [32] Joiner N, Hirose A and Dorland W 2010 *Phys. Plasmas* **17** 072104
- [33] Hong B G, Horton W and Choi D I 1989 *Plasma Phys. Control. Fusion* **31** 1291
- [34] Siena A et al 2018 *Nucl. Fusion* **58** 054002
- [35] Zhang W L, Lin Z H and Chen L 2011 *Phys. Rev. Lett.* **107** 239501
- [36] Brizard A J and Hahm T S 2007 *Rev. Mod. Phys.* **79** 421
- [37] Holod I et al 2009 *Phys. Plasmas* **16** 122307
- [38] Parker S E and Lee W W 1993 *Phys. Fluids B* **5** 77
- [39] Porazik P and Lin Z H 2011 *Commun. Comput. Phys.* **10** 899
- [40] Lee W W 1987 *J. Comput. Phys.* **72** 243
- [41] Tobias B J et al 2011 *Phys. Rev. Lett.* **106** 075003
- [42] Deng W J and Lin Z H 2009 *Phys. Plasmas* **16** 102503
- [43] Lin Z and Hahm T S 2004 *Phys. Plasmas* **11** 1099